

AN ATTEMPT TO EVALUATE PRESSURE FORCE ON A FLAPPING RIGID PLATE USING VELOCITY DATA OF PIV MEASUREMENTS

Alexandre Suryadi^{1,2} and Shinnosuke Obi¹

¹ Department of Mechanical Engineering, Keio University, Yokohama, Japan
Tel: 81-45-566-1499, Fax: 81-45-566-1495, e-mail: obsn@mech.keio.ac.jp

² Linné Flow Centre, Department of Mechanics, Royal Institute of Technology, Stockholm, Sweden
Tel: 46-8-790-7582, e-mail: alexandre@mech.kth.se

Received: February 9, 2012

Abstract

The flow field generated by a sinusoidally flapping rigid flat plate was measured using stereo particle image velocimetry to estimate the pressure field on two cross sections of the flapping plate. The pressure field was estimated by integrating the three-dimensional Poisson equation derived from the Euler equation. The solution of this Poisson equation is obtained as a function of the measured phase-averaged velocity field. Simultaneous to PIV measurements, the torque on the flapping axis, which depicts the forces acting on the wing, was measured using strain gauges. The maximum torque coefficients, observed from both methods, of each cycle are delayed from the maximum acceleration of the plate at $\hat{\phi}=0.25$ and $\hat{\phi}=0.75$, with $\hat{\phi}$ being the relative phase angle. One of the factors of the phase delay is attributed to the separation of vortex structure along the edges of the plate. After the separation point the increase of pressure drag is delayed relative to the flapping motion, $\hat{\phi}=0.35$. At the same phase, vortex structure is generated on the leeward side of the plate at the free end. Low pressure region was observed on the leeward side of the plate which further adds to the pressure drag.

Keywords: Flapping wing, Pressure estimation, Stereo PIV, Vortex-structure interaction, Wake-capture

Introduction

The desire to understand the aerodynamics of insect flight has motivated the engineering of a micro-air vehicle (MAV) with flapping propulsion [1,2,3,4,5,6,7]. An MAV is defined as an autonomous flying vehicle with length, width and height less than 15 cm [8]. Its main function is as a platform for observations in close proximity or over an obstructed field of view of the operator. To match its source of motivation, an insect or a bird, the design of an MAV requires it to produce lift and thrust simultaneously, hover, and autonomously control its flight while efficiently interacting with nature to have stable flight. These design objectives require the innovation of flexible and lightweight materials, autonomous flight control by using sensors placed on the body of the MAV and minimal power consumption from on-board batteries. In this paper, the fluid physics of flapping flight will be discussed through a set of measurements to elucidate the generation of aerodynamic force of a flapping wing model. In the study of flapping wing aerodynamics, the flight behavior of insects has become the source of inspiration due to its relatively simpler wing kinematics than that of birds. The kinematics of the wings of an insect has been modeled in full or in reduced form. From a continuous motion of a wing that flaps at a constant frequency and

amplitude, each flapping cycle is decomposed into an upstroke and a downstroke motion. Each stroke can be decomposed further into the translation phase, where the flapping wing is moving forward, and the reversal phase, where the wing rotates supinely or pronately then moves in the reverse direction to complete a full stroke. The reversal phase is particularly interesting because at this phase the wing has little forward velocity. With little forward velocity, the generation of force on the wing is explained through wing–rotation and wake–capture mechanism [3].

The generation of force during wing–rotation is due to the production of circulation to fulfill the Kutta condition on the trailing edge of the wing: A phenomena called Wagner effect or rotational forces [9]. After the rotation of the wing, the wing accelerates and encounters the wake generated from the previous stroke. Vorticity in the wake induces the fluid at rest to flow and collide with the wing. This flow has been called inter–vortex stream. The impingement of the flow by the flapping plate contribute significantly to the increase of force acting on the wing, whether the wing is accelerated or not. Flow visualization studies have also revealed that the shed wake and its interaction with the wing [3, 9, 10].

The source of aerodynamic force is the pressure difference on each surface of a body. The evaluation of pressure difference requires the information from the pressure field, which is difficult to measure at various points simultaneously. The methods for force prediction by PIV imaging were proposed, which substitutes the pressure term in the momentum equation with the integration of the Navier–Stokes equation [11], and through mathematical manipulations, which expresses the pressure term in the momentum equation solely by the velocity fields [12]. These methods approximate the force vector on a flapping wing or bluff body by integrating a control volume in the velocity field. Alternatively, the pressure field can be estimated by integrating the discrete formulation of the Poisson equation constructed from the phase-averaged velocity field [13, 14, 15]. With the estimated pressure field, the relation of pressure and vorticity can be observed.

In this study, the wing was simplified as a flat plate and it was assumed to be rigid for the duration of the flapping motion. The flapping motion is sinusoidal about the chordwise axis. There is no rotation about the spanwise axis of the flapping plate, so that the force generation in the reversal phase is generated solely by wake–capture. Instantaneous velocity fields were measured using stereo particle image velocimetry (PIV) and for the analysis of unsteady motion, the instantaneous velocity fields were phase–averaged according to the flapping angle. This paper solely covers the evolution of the vorticity field and its effect to the pressure distribution about the reversal phase. The calculation of force based on the integration of the pressure distribution is discussed in [14] and [15].

Measurement Setup and Parameters

The measurement setup and parameters were similar to those in [14] and described in detail in [15]. The wing was modeled with a plate made of acrylic that was 40 mm in span length, b , and 20 mm in chord length, c . The thickness of the plate was 2 mm and during the calibration process of the flapping actuators, the plate maintained its rigidity on every flapping phase. The flapping kinematics was simplified as a single axis under sinusoidal motion,

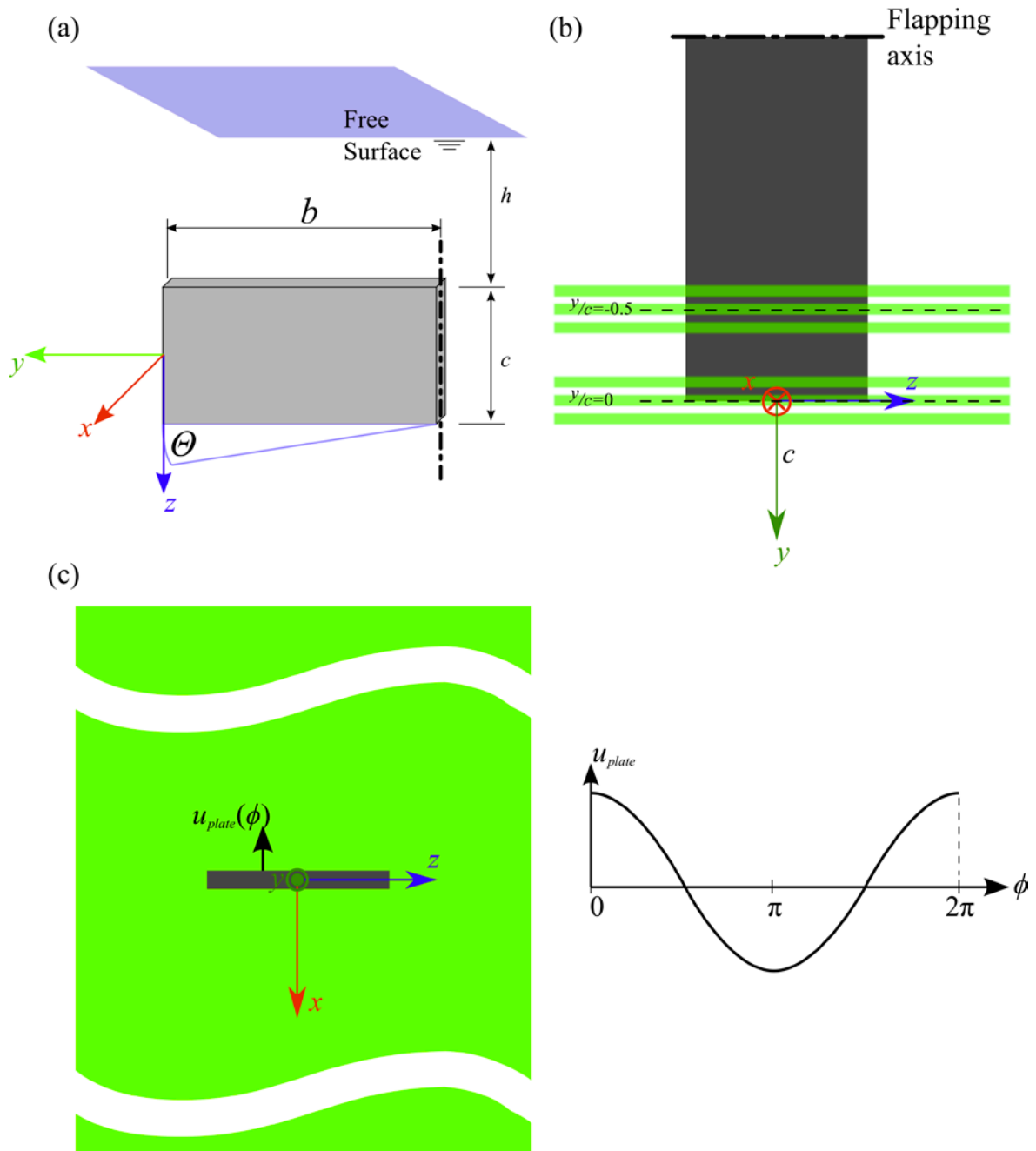


Figure 1. (a) measurement setup and parameters (b) locations of the laser sheet relative to the flapping plate at rest (c) the locations of the flapping plate relative to a laser sheet, this view orientation will be used to explain the result in succeeding sections of this paper

$$\theta(t) = \Theta \sin(2\pi ft) \quad (1)$$

$$x = r \cos(\theta) \quad (2)$$

$$y = r \sin(\theta) \quad (3)$$

where θ is the flapping angle and $\Theta = \max(\theta) = 18^\circ$, f is the flapping frequency in Hz, r is along the span of the plate, and x, y are the location of the plate in Cartesian form. The measurement parameters and orientation of x, y , and z are given in Figure 1(a). The term windward surface represents the surface of the plate facing the flow and leeward surface the opposite side. The flapping phase is defined as $0 \leq \hat{\phi} < 1$, where $\hat{\phi} = 1$ indicates one

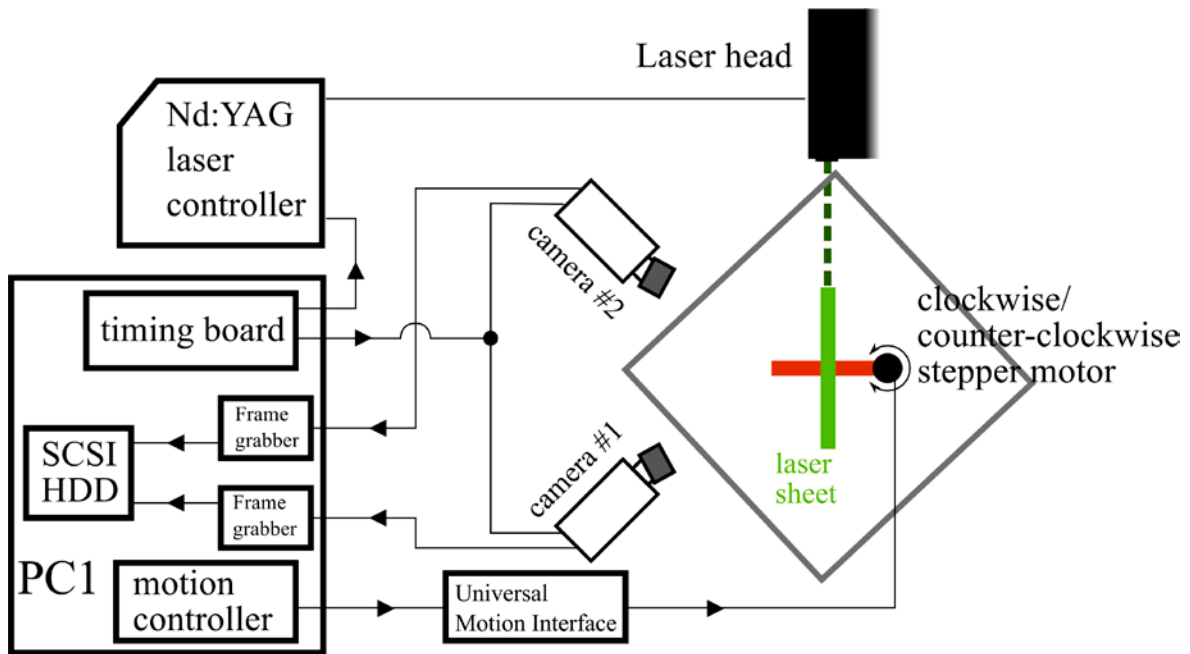


Figure 2. Stereo PIV arrangement

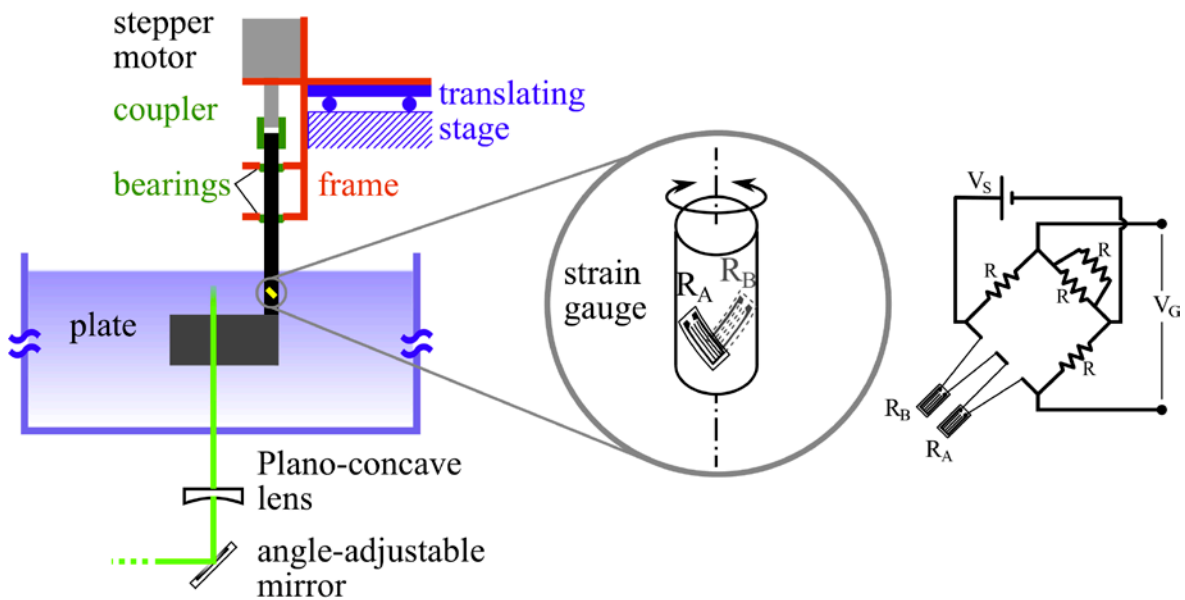


Figure 3. Arrangement of the flapping actuator and of torque measurement using strain gauges

flapping cycle or when $\theta(t)$ completes one period. The flapping phase was discretized into 20 discrete phases represented by $\hat{\phi} = 0, 0.05, 0.10, \dots, 0.95$. The flow Reynolds number is,

$$\text{Re} = \frac{U(b\Theta)}{\nu} \quad (4)$$

where $U = \max(\dot{\theta}b)$ is the maximum velocity of the plate, $b\Theta$ is the flapping amplitude, and ν is the dynamic viscosity of water. The flow was measured with stereo PIV at $f = 2$ Hz,

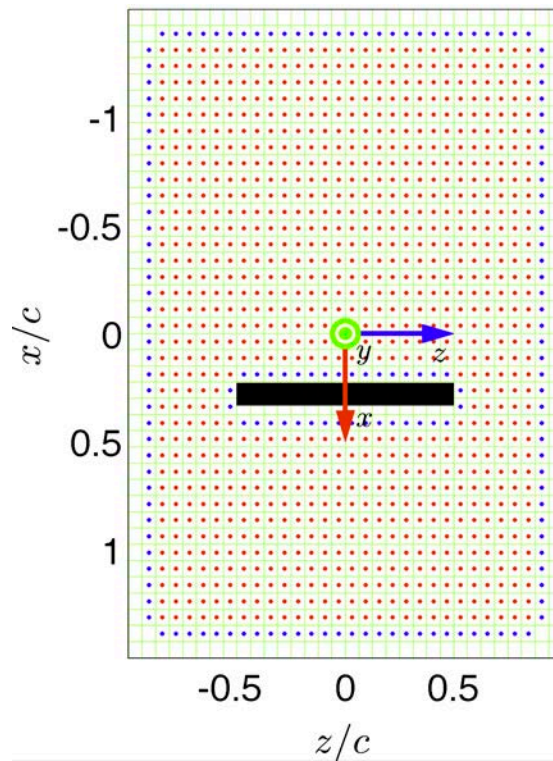


Figure 4. Definition of the mesh for the estimation of pressure from phase-averaged velocity field measured using PIV. The plate is $\hat{\phi} = 0.25$. The mesh is defined for each $\hat{\phi}$

which gives $Re = 3160$. This Reynolds number was selected because it is in the flight operational range of insects.

The stereo PIV measurement setup is shown in Figure 2 and the flapping system and torque measurement system arrangement is shown in Figure 3. The stereo PIV measurement was conducted with two Redlake Megaplus ES1.0 camera with 1018×1008 pixel sensor area. The measurement was conducted for the $3c \times 2c$ area around the plate. The plate was submerged $5c$ under the surface of water in a transparent tank. The walls of the tank were approximately $7c$ away from every direction of the plate. The location of the flapping plate relative to walls of the tank and free surface in this setup is sufficient to approximate an infinite volume [3].

A clockwise/counter-clockwise stepper motor directly drove the flapping plate. The motor axis was joined to the flapping axis with a jaw coupler to reduce vibrations. One of the ends of the plate was fixed to the flapping axis and the other end was free. These components were constructed on a movable frame for measuring the flow on different sections of the plate. A laser sheet was produced from the Nd:YAG Solo II laser system. Its laser beam was passed through a plano-concave lens to illuminate a planar layer of the flow, parallel to the xz -plane. Three layers were measured to approximate all elements of the deformation tensor. These layers were set 2 mm apart at $y = -8, -10, \text{ and } -12$ mm and at $y = -2, 0, \text{ and } 2$ mm (cf. Figure 1(b)). Additionally, the work of [16] was used to visualize the vortex structure, quantitatively, through the stereo PIV measurement on three planar layers at $z = 0, 5, \text{ and } 10$ mm parallel to the xy -plane around the free end of the flapping plate. Three velocity components of each layer were reconstructed using a third-order polynomial and calibration data [17]. The location of the flapping plate relative to a laser sheet is shown in Figure 1(c).

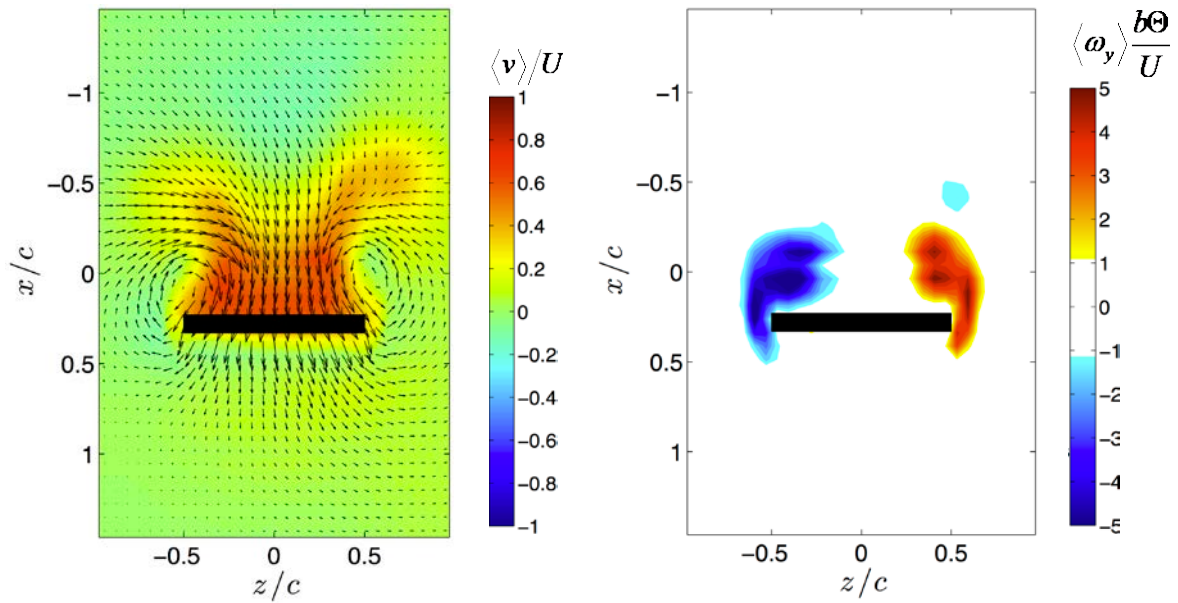


Figure 5. The cross section of the flow generated by a flapping plate at $y/c = -0.5$ for $\hat{\phi} = 0.6$. The cross section of the plate is depicted as the black square. (a) Phase-averaged velocity field; vectors indicate $\langle \mathbf{u} \rangle / U$, $\langle \mathbf{w} \rangle / U$ and the color indicates $\langle \mathbf{v} \rangle / U$. (b) Vorticity in the y-direction, color indicates $\langle \omega_y \rangle (b\Theta) / U$

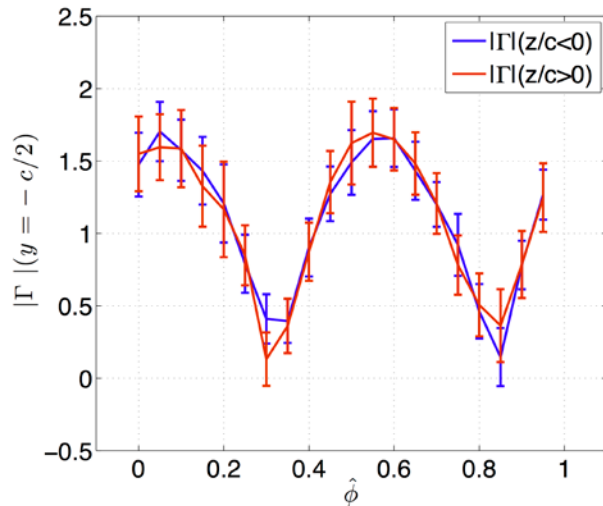


Figure 6. Symmetry examination of the vortex flow on the spanwise plane, $y/c = -0.5$, analyzed with the normalized circulation of either side of the centerline, $z/c = 0$

This view orientation will be used to present the important results in this paper.

Two strain gauges R_A and R_B were attached diametrically opposite of each other on the surface of the flapping axis (cf. Figure 3). Changes in torsion load cause the changes of resistance, ΔR_A and ΔR_B for R_A and R_B , respectively. These changes were registered by the voltage V_G as,

$$V_G = \frac{\Delta R_A + \Delta R_B}{3R} V_s \quad (5)$$

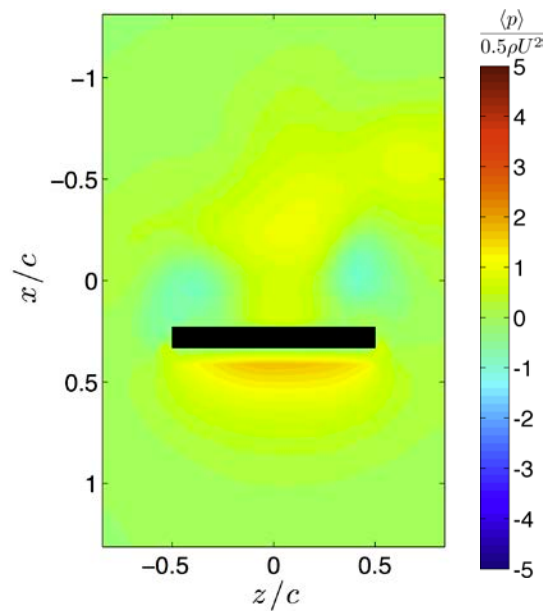


Figure 7. Estimation of the pressure field generated by a flapping rigid plate (black line) on the spanwise plane at $y/c = -0.5$ and $\hat{\phi} = 0.60$

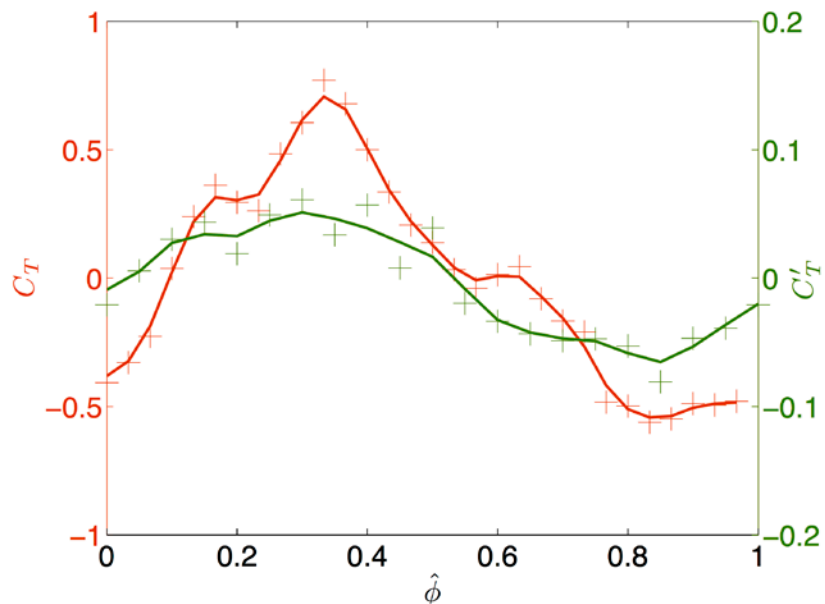


Figure 8. Phase-averaged torque generated by the flapping plate measured on the flapping axis for $Re=3160$. Markers by “+” indicate unfiltered data and solid lines indicate data filtered with moving average

where R is the resistance of the bridge and V_S is the input voltage. The strain gauges were submerged in water and a rubber coating was painted on them to make them water proof [18]. With the wing removed, the registered signal exhibits high frequency and very low amplitude signal, which is considered as measurement noise. Torque measurements were done simultaneously with stereo PIV measurements.

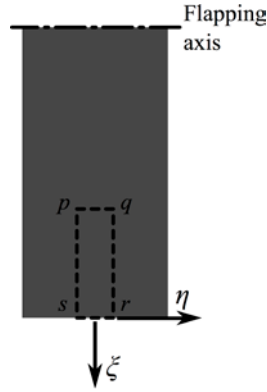


Figure 9. The control surface, “pqrs” to calculate torque from pressure estimates. $pq = 2$ mm and $ps = 2$ mm. The coordinate system ξ, η is defined on the surface of the plate

Pressure Estimation

The estimation of the pressure force acting on the plate surface was conducted in the same way as is given in [15]. The pressure field was approximately obtained by solving the three-dimensional Poisson equation formulated using the phase-averaged velocity field. The phase-averaged velocity field, $\langle \mathbf{u} \rangle$, was calculated from $N = 500$ set of instantaneous velocity fields, $\langle \mathbf{u}' \rangle$, for each $\hat{\phi}$, measured using stereo PIV:

$$\langle \mathbf{u} \rangle(\mathbf{x}, \hat{\phi}) = \frac{1}{N} \sum_{n=1}^N \mathbf{u}[\mathbf{x}, (n+2\pi\hat{\phi})/f] \quad (6)$$

The deformation tensor, including the out-of-plane deformations, was calculated using the second-order finite difference approximation. To calculate the out-of-plane deformation, the stereo PIV's measurement planes were shifted by 2 mm in the normal direction of the measurement plane. The pressure was solved on selected nodes on the stereo-PIV velocity field indicated by the red dots in Figure 4. The cross-section of the flapping plate and the measurement plane is shown as the black square from $-0.5 \leq z/c \leq 0.5$.

The phase-averaged velocity field is, $\langle \mathbf{u} \rangle = (\langle u \rangle, \langle v \rangle, \langle w \rangle)$, and the fluctuating velocity, $\mathbf{u}' = (u', v', w')$, where $\mathbf{u}' = \mathbf{u} - \langle \mathbf{u} \rangle$. After applying the continuity condition, the phase-averaged Poisson equation is

$$\begin{aligned} \frac{\partial^2 \langle p \rangle}{\partial x^2} + \frac{\partial^2 \langle p \rangle}{\partial y^2} + \frac{\partial^2 \langle p \rangle}{\partial z^2} = & -\rho \left[\left(\frac{\partial \langle u \rangle}{\partial x} \right)^2 + \left(\frac{\partial \langle v \rangle}{\partial y} \right)^2 + \left(\frac{\partial \langle w \rangle}{\partial z} \right)^2 \right. \\ & + 2 \left(\frac{\partial \langle u \rangle}{\partial y} \frac{\partial \langle v \rangle}{\partial x} + \frac{\partial \langle u \rangle}{\partial z} \frac{\partial \langle w \rangle}{\partial x} + \frac{\partial \langle v \rangle}{\partial z} \frac{\partial \langle w \rangle}{\partial y} \right) + \left(\frac{\partial^2 \langle u' u' \rangle}{\partial y^2} + \frac{\partial^2 \langle v' v' \rangle}{\partial z^2} + \frac{\partial^2 \langle w' w' \rangle}{\partial z^2} \right) \\ & \left. + 2 \left(\frac{\partial^2 \langle u' v' \rangle}{\partial y \partial x} + \frac{\partial^2 \langle u' w' \rangle}{\partial z \partial x} + \frac{\partial^2 \langle v' w' \rangle}{\partial z \partial y} \right) \right] \quad (7) \end{aligned}$$

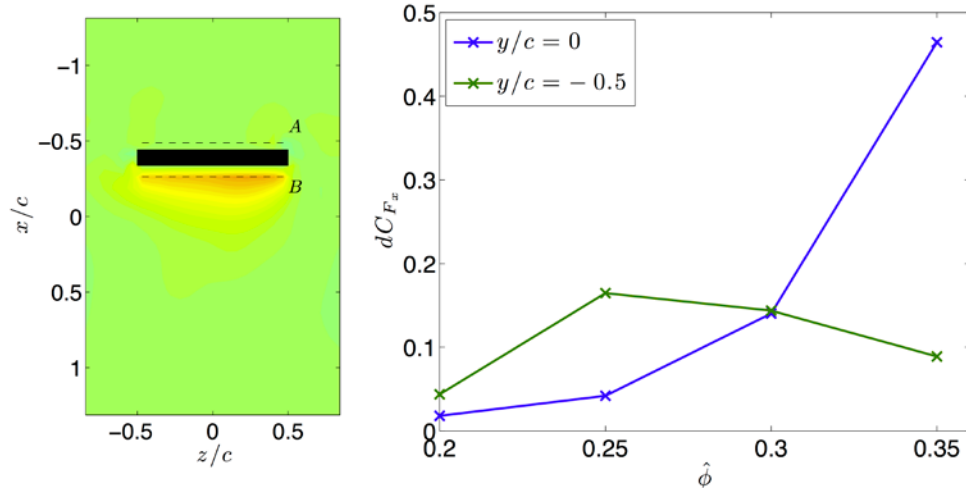


Figure 10. (a) approximation of the pressure difference on the surface of the plate (b) sectional force coefficient in the x-direction, dC_{F_x} , an approximation of the sectional force coefficient on the surface of the plate

and in this study Equation (7) was solved using the Gauss-Seidel iterative method. On the perimeter of the mesh and around the flapping plate, shown as blue dots in Figure 4, the Neumann boundary condition (pressure gradient) was applied to Equation (7); the pressure gradient was calculated using the Euler equation from the phase-averaged velocity field. Because the grid is in x, y, z coordinate, the boundary conditions are,

$$\frac{\partial \langle p \rangle}{\partial x} = -\rho \left[\frac{\partial \phi}{\partial t} \frac{\partial \langle u \rangle}{\partial \phi} + \left(\langle u \rangle \frac{\partial \langle u \rangle}{\partial x} + \langle v \rangle \frac{\partial \langle u \rangle}{\partial y} + \langle w \rangle \frac{\partial \langle u \rangle}{\partial z} \right) + \left(\frac{\partial \langle u'u' \rangle}{\partial x} + \frac{\partial \langle u'v' \rangle}{\partial y} + \frac{\partial \langle u'w' \rangle}{\partial z} \right) \right] \quad (8)$$

$$\frac{\partial \langle p \rangle}{\partial y} = -\rho \left[\frac{\partial \phi}{\partial t} \frac{\partial \langle v \rangle}{\partial \phi} + \left(\langle u \rangle \frac{\partial \langle v \rangle}{\partial x} + \langle v \rangle \frac{\partial \langle v \rangle}{\partial y} + \langle w \rangle \frac{\partial \langle v \rangle}{\partial z} \right) + \left(\frac{\partial \langle u'v' \rangle}{\partial x} + \frac{\partial \langle v'v' \rangle}{\partial y} + \frac{\partial \langle v'w' \rangle}{\partial z} \right) \right] \quad (9)$$

$$\frac{\partial \langle p \rangle}{\partial z} = -\rho \left[\frac{\partial \phi}{\partial t} \frac{\partial \langle w \rangle}{\partial \phi} + \left(\langle u \rangle \frac{\partial \langle w \rangle}{\partial x} + \langle v \rangle \frac{\partial \langle w \rangle}{\partial y} + \langle w \rangle \frac{\partial \langle w \rangle}{\partial z} \right) + \left(\frac{\partial \langle u'w' \rangle}{\partial x} + \frac{\partial \langle v'w' \rangle}{\partial y} + \frac{\partial \langle w'w' \rangle}{\partial z} \right) \right] \quad (10)$$

The derivatives were approximated by second-order finite difference scheme. Convergent result was defined when the rate of the residual reached 0.01 of its initial value.

The random error or the uncertainty of the measured velocity field is represented by the standard deviation of the velocity, σ_{u_i} . Using the estimate of σ_{u_i} , $s_{u_i} = (n-1)^{-1} \sqrt{\sum (u_i - \bar{u}_i)^2}$. Where, n is the number of sample and $\langle u_i \rangle$ is the sample mean of u_i . The precision of the measurement is $P_{u_i} = t_{n,\alpha/2} s_{u_i}$ [19]. The average precision limits of each velocity component evaluated for the confidence interval $\alpha = 95\%$ are $P_u = 0.03U$, $P_v = 0.03U$, and $P_w = 0.05U$.

The uncertainties of the velocity components are propagated through the integration of Equation (7). The uncertainty of $\langle p \rangle$ is,

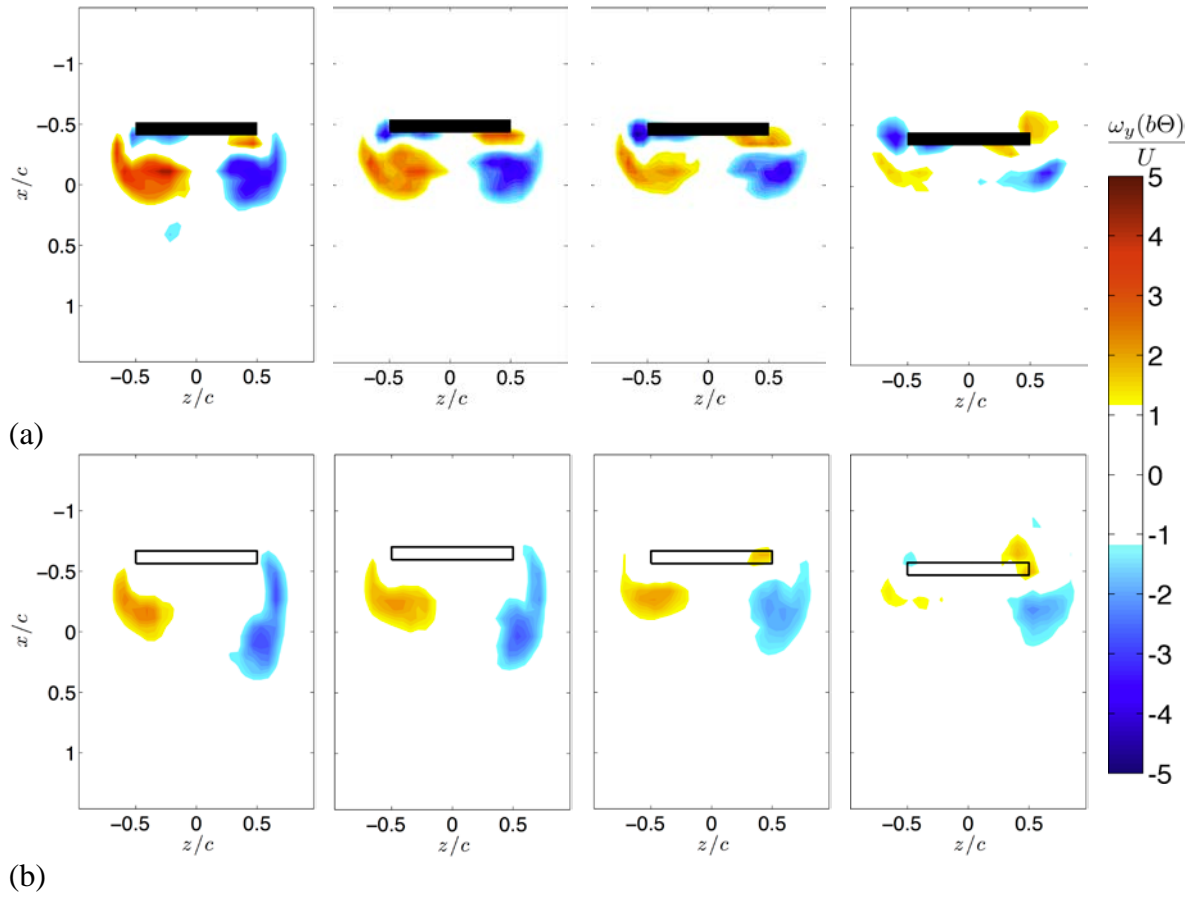


Figure 11. Vorticity, $\langle \omega_y \rangle (b\Theta)/U$, generated by a flapping plate (square) on the xz cross-section at (a) $y/c = -0.5$ and (b) $y/c = 0$ for $\hat{\phi} = 0.20$, $\hat{\phi} = 0.25$, $\hat{\phi} = 0.30$, and $\hat{\phi} = 0.35$ from left to right

$$s_{(p)}^2 = \left(\frac{\partial \langle p \rangle}{\partial x} \left(\frac{\partial \langle x \rangle}{\partial u} s_{(u)} + \frac{\partial \langle x \rangle}{\partial v} s_{(v)} + \frac{\partial \langle x \rangle}{\partial w} s_{(w)} \right) \right)^2 + \left(\frac{\partial \langle p \rangle}{\partial y} \left(\frac{\partial \langle y \rangle}{\partial u} s_{(u)} + \frac{\partial \langle y \rangle}{\partial v} s_{(v)} + \frac{\partial \langle y \rangle}{\partial w} s_{(w)} \right) \right)^2 + \left(\frac{\partial \langle p \rangle}{\partial z} \left(\frac{\partial \langle z \rangle}{\partial u} s_{(u)} + \frac{\partial \langle z \rangle}{\partial v} s_{(v)} + \frac{\partial \langle z \rangle}{\partial w} s_{(w)} \right) \right)^2 \quad (11)$$

The average uncertainty of the pressure is $P_p = t_{n,df2} s_p = 6.60$ or 0.54 of the reference pressure, $1/2 \rho U^2$, although the properness of the approximated pressure field strongly depends on the nature of the flow field.

Results

Phase-Averaged Velocity Field

A representation of the flow field generated by a flapping plate is shown by the phase-averaged velocity vectors at $\hat{\phi} = 0.60$ in Figure 5(a). The flapping plate is illustrated by the black square, velocity vectors represent $\langle \mathbf{u} \rangle / U$, $\langle \mathbf{w} \rangle / U$, and the color represents $\langle v \rangle / U$. The cross section at $y/c = -0.5$ was selected. At $\hat{\phi} = 0.60$, the plate is moving to the positive x -direction; rotational parts of the flow can be observed on the edges of the plate.

On the leeward surface of the plate, $\langle \mathbf{v} \rangle$ is toward the free end of the plate and $(\langle \mathbf{u} \rangle, \langle \mathbf{w} \rangle)$ are toward the plate. On the windward surface the plate pushed the bulk of fluid away.

The distribution of vorticity in the y -direction of Figure 5(a) is given in Figure 5(b). A pair of counter-rotating vortices is observed on the edges of the plate as evident by the rotational flow in Figure 5(a). This pair is part of one continuous three-dimensional vortical structure on the edges of the plate. It is generated and dragged with the plate along during the flapping motion.

Flow Symmetry

Symmetry of the vortex flow over the centerline, $z/c=0$, is observed throughout the flapping phase in Fig. 6. The normalized circulation on the plane at $z/c=-0.5$ is given by $|\Gamma| = \left| \left(\int_A \langle \omega_y \rangle dA \right) / (Ub\Theta) \right|$ for $y/c=-0.5$ and the vertical bars are the precision errors of Γ . From this figure, the flow can be considered symmetrical. Although the averaged values of $|\Gamma|$ shows a deviation from symmetry, most notably at $\hat{\phi} = 0.30$ and $\hat{\phi} = 0.85$, they are considered to be within the precision error.

The local maxima of $|\Gamma|$ are at $\hat{\phi} = 0.05$ and $\hat{\phi} = 0.55$, delayed after the mid-stroke of the flapping motion. And the local minima are at $\hat{\phi} = 0.30$ and $\hat{\phi} = 0.85$, because of the existence of a new pair of vortices with opposing strength on the surface of the plate, which will be discussed in the next section.

Estimated Pressure

The estimation of pressure of the velocity field in Figure 5(a) is shown in the form of pressure coefficient, $C_p = \langle p \rangle / (1/2 \rho U^2)$, in Figure 7. The cross section of the flapping plate with the measurement plane is shown as the black line moving in the positive x -direction. The pressure field in Figure 7 is not to be mistaken to be a snapshot of the evolution of the wake generated behind the flapping plate. This is because Equation (7) is independent of time as the right hand side consists of only the spatial derivatives of the velocity field.

The pressure distribution in Figure 7 shows a large stagnation area on the windward surface and a smaller one on the leeward surface of the plate. The smaller stagnation area is in between two lower pressure regions, associated with the presence of vorticity as shown in Figure 5(b).

Discussion

The forces generated by the flapping wing were evaluated as the torque acting on the flapping axis shown in Figure 8. Two methods were used to estimate such torque: measurement using strain gauges and the integration of the pressure distribution on the surface of the plate evaluated from PIV velocity fields. The latter, “pressure” method, C_T' , is evaluated on a smaller portion of the plate compared to the former, “gauge”, method, C_T : 2mm × 12.5mm along the chord and radial direction relative to the surface of the plate compared to 20mm × 40mm full area of the plate. The calculation of torque from pressure estimates is illustrated in Figure 9 and formulated in Equation 12, where the coordinates ζ and η are defined on the surface of the plate.

$$T(z) = \int_P \int_P (\eta \langle p \rangle \hat{n}_\zeta + \zeta \langle p \rangle \hat{n}_\eta) d\eta d\zeta \quad (12)$$

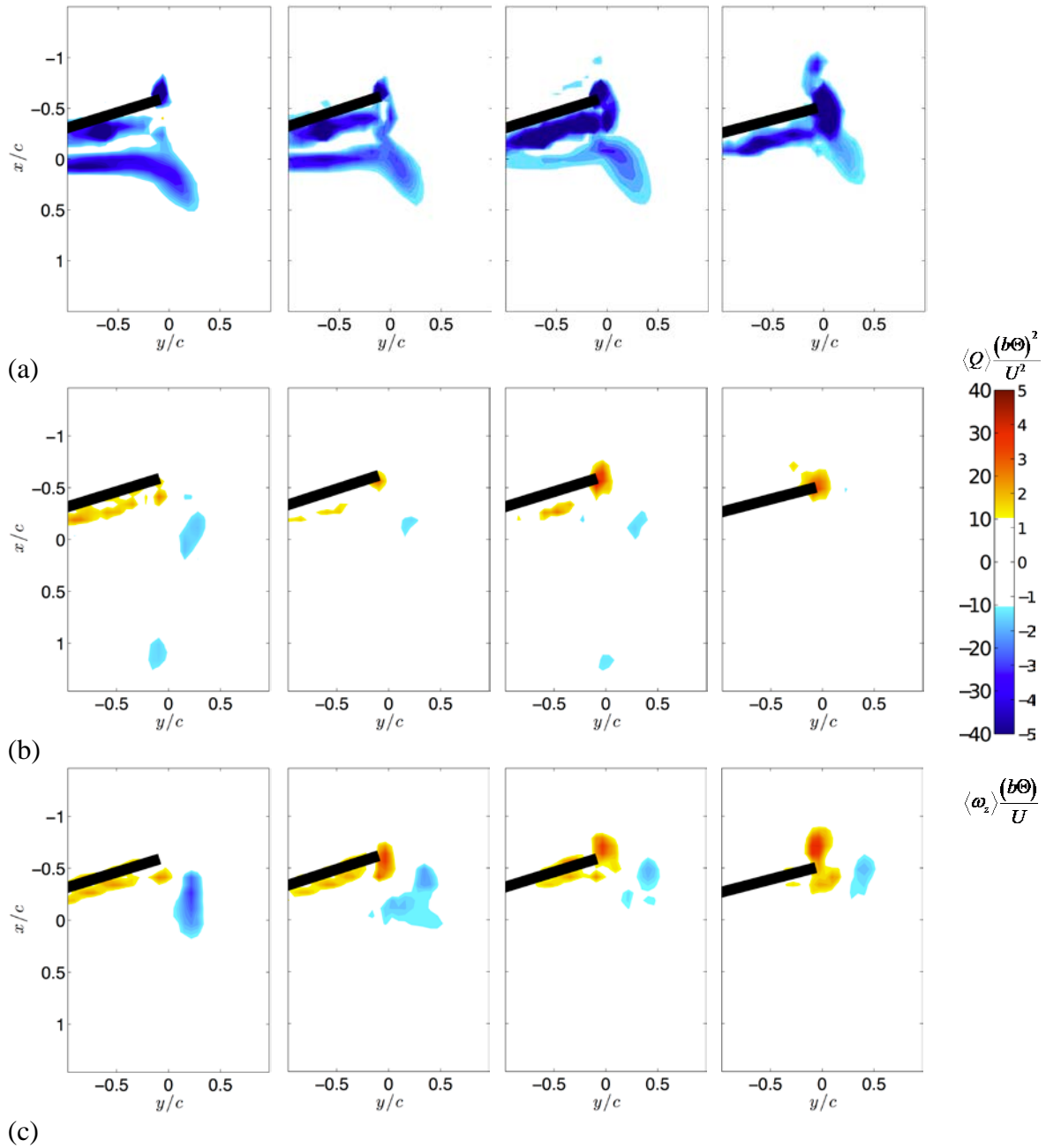


Figure 12. (a) the vortex structure for the chordwise cross-section at $z/c = 0.5$ and the vorticity in z -direction at (b) $z/c = 0.5$ and (c) $z/c = 0$ for $\hat{\phi} = 0.20$, $\hat{\phi} = 0.25$, $\hat{\phi} = 0.30$, and $\hat{\phi} = 0.35$ from left to right. The vortex structure is highlighted by the method described Hunt et al. [20], which ranges from $-40 \leq \langle Q \rangle (b\theta/U)^2 \leq 40$. The vorticity strength ranges from

$$-5 \leq \langle \omega_z \rangle (b\theta)/U \leq 5 \text{ [16]}$$

The phase-averaged torque in Figure 8 is filtered using a moving average filter (line) and the unfiltered data is given by “+” markers. Figure 8 shows the maximum torque coefficients at $\hat{\phi} \approx 0.35$ and $\hat{\phi} \approx 0.85$. In other words, the increase of torque coefficients occurs after the start of every reverse stroke, where in this study, after the maximum acceleration of the plate.

Despite the difference between the two methods, they are qualitatively similar; maximum torque is produced at a delayed phase relative to the acceleration of the plate.

It is not possible to estimate the pressure distribution on the surface of the plate because the plate is not oriented normally to the cross-section. Instead, the pressure difference is approximated at points along y/c closest to each surface of the plate. Figure 10(a) illustrates the location of those points. The sectional force coefficients in the x -direction, dC_{F_x} is approximated,

$$dC_{F_x} = \frac{\Delta y \Delta z \sum_i^N (P_{A_i} - P_{B_i})}{1/2 \rho U^2} \quad (13)$$

where $\Delta y = 2$ mm and $\Delta z = 1.25$ mm. In Figure 10(b), dC_{F_x} on $y/c = -0.5$ shows the maximum pressure difference occurring at $\hat{\phi} = 0.25$ and decreases in the succeeding phase angles. While dC_{F_x} on $y/c = 0$, increases from $\hat{\phi} = 0.20$ to a maximum at $\hat{\phi} = 0.35$, the magnitude of the maximum dC_{F_x} on $y/c = 0$ is approximately 300% of that on $y/c = -0.5$. The phase delay is more prominent on the outer span than on the inner span of the flapping plate. The source of the phase delay can be observed from the distribution of vorticity in Figure 11.

The vorticity distribution, ω_y , in Figure 11 is shown for the cross section at (a) $y/c = -0.5$ and (b) $y/c = 0$. The local position of the plate is illustrated as the black square in Figure 11(a) and as the empty square in Figure 11(b). The latter is to illustrate the projection of the plate to the measurement plane. The vorticity distribution in Figure 11(a) at $\hat{\phi} = 0.20$ shows the interaction of a vortex pair created during the previous flapping stroke with the leeward surface of the plate causing the formation, on the surface, of secondary vortex pair with opposite strength to that of the primary one. The vorticity distributions in the succeeding phases show the reversal of the motion of the flapping plate starting from $\hat{\phi} = 0.25$. Both primary and secondary vortex pairs are diffused outward of the plate with the primary one decaying. The interaction between the vortices and plate on the cross section at $y/c = -0.5$ gives a pressure difference response that is in the same phase with the flapping motion.

The vortex pair in Figure 11(b), with the extension of the vortex pair of Figure 11(a) to the xz -plane at $y/c = 0$, is located farther from the plate due to the separation point located on the spanwise of the plate [2, 16]. Judging from the shape of the vortex pair, its interaction with the plate occurs at $\hat{\phi} = 0.35$. This separation of the vortex pair from the surface of the plate at $y/c = 0$ is an essential point to the phase delay observed in Figure 8.

The delay of vortex–structure interaction along the span is best observed in Figure 12(a), where the vortical structure on the cross section parallel to xy -plane at $z/c = 0.5$ is highlighted by calculating the second invariance of the deformation tensor, $\langle Q \rangle = -(\partial \langle u_i \rangle / \partial x_j)(\partial \langle u_j \rangle / \partial x_i) - (\partial \langle u_i' u_j' \rangle / \partial x_j \partial x_i)$, with $i, j = 1, 2, 3$. A vortex is positively identified when $\langle Q \rangle < 0$ [20]. In this figure, $\langle Q \rangle$ best describes the vortex structure because the vortex line is parallel to the cross-section. The vortical structure at $\hat{\phi} = 0.20$ shows a separation point at approximately $0.25c$ behind the free end of the flapping plate. The reverse flapping motion starts at $\hat{\phi} = 0.25$ and the interaction of the vortical structure with the flapping plate starts from the inner span section of the plate moving closer to the free end with succeeding phases, as shown by the distribution of the strength of $\langle Q \rangle$. At $\hat{\phi} = 0.35$, a vortical structure attached to the free end is produced on the leeward surface of the plate.

The vorticity in the z -direction is given in Figure 12(b)–(c) for the cross-section at $y/c = 0.5$ and $y/c = 0$, respectively. In Figure 12(b), positive $\langle \omega_y \rangle$ dominates on the surface of the plate. At $\hat{\phi} = 0.30 - 0.35$, $\langle \omega_z \rangle$ is observed on the free end of the plate. In Figure 12(c), two vortices are observed at $\hat{\phi} = 0.25$. One attached to the free end of the plate and the other separated from the surface of the plate. On the succeeding phase angles, with the interaction of the vortical structure in Figure 12(a) with the plate, the separated vortex moves closer relative to the plate. The vortex attached to the free end grows and envelopes the leeward side of the free end at $\hat{\phi} = 0.35$. In addition to stagnation on the windward surface, the vortex attached at the free end of the plate as observed in Figure 12(b)–(c) at $\hat{\phi} = 0.35$ may contribute to the increase of pressure difference by creating a suction zone on the leeward surface of the plate.

Conclusions

The present paper discussed on the experimental method to evaluate the pressure force acting on a flapping rigid plate by using velocity data measured by a stereo PIV. The measurement of velocity field and phase-averaged analysis showed the evolution of the phase-averaged vortical structures during a flapping cycle. The integration of the Poisson equation from a measured velocity field reasonably approximated the pressure field on the spanwise sections of the plate in a single-axis sinusoidal flapping. The relation of the torque of the flapping axis with vorticity was investigated through several slices of the vorticity and pressure distribution.

On the onset of the reversal of the flapping motion, vortex structures impinge on the plate at $y/c = -0.5$, which produces a secondary vortex structure on the surface of the plate with opposite rotation. The response of pressure difference at $y/c = -0.5$ is in the same phase with the flapping motion. The impingement of the flow by the plate diffuses the vortex structure around the edges of the plate.

Vorticity distribution near the free end of the plate, approximated at the cross-section $y/c = 0$, shows that the flow impingement occurs at $\hat{\phi} = 0.35$, phase delayed relative to the flapping motion. The delay is caused by the separation of the vortex structure on the edge of the plate before its free end. At $\hat{\phi} = 0.35$, the impingement of vortex structure produces stagnation area on the windward surface. The significant increase of pressure difference at this cross-section may also be attributed to the growth of the vortex structure attached to the free end, which produces a suction area on the leeward side of the plate.

The mechanism that generates pressure force on the plate was well correlated with the generation of the vortex motion. The present methodology may be extended to the analysis of fluid-structure interaction in more complex situation including that of flexible structure.

Acknowledgement

The present work has been supported by a research fund provided by the Keio Leading-edge Laboratory. The financial support for the first author through MEXT Scholarship is greatly acknowledged. The authors are grateful to Dr. Y. Naka for his assistance in conducting experiments and to Prof. K. Fukagata for valuable discussions.

References

- [1] A. Azuma, *The Biokinetics of Flying and Swimming*, American Institute of Aeronautics and Astronautics, Springer-Verlag, New York, United States, 1992.

- [2] C.P. Ellington, C.V.D. Berg, A.P. Willmott, and A.L. Thomas, "Leading-edge vortices in insect flight," *Nature*, Vol. 384, pp. 626–630, 1996.
- [3] M.H. Dickinson, F.O. Lehmann, and S.P. Sane, "Wing rotation and the aerodynamic basis of insect flight," *Science*, Vol. 284, pp.1954–1960, 1999.
- [4] C.P. Ellington, "The novel aerodynamics of insect flight: Applications to micro-air vehicles," *The Journal of Experimental Biology*, Vol. 202, pp. 3439–3448, 1999.
- [5] K.D. Jones, S.J. Duggan, and M.F. Platzer, "Flapping-wing propulsion for a micro air vehicle," In: *AIAA, 38th Aerospace Sciences Meeting and Exhibit*, Aerospace Sciences Meetings, 2001.
- [6] M.F. Platzer, K.D. Jones, J. Young, and J.C. Lai, "Flapping-wing aerodynamics: Progress and challenges," *AIAA Journal*, Vol. 46, No. 9, pp. 2136–2159, 2008.
- [7] K.D. Jones, and M.F. Platzer, "Design and development considerations for biologically inspired flapping-wing micro air vehicles," *Experiments in Fluids*, Vol. 46, No. 5, pp. 799–810, 2009.
- [8] J.M. McMichael, and M.S. Francis, "Micro Air Vehicles – Toward A New Dimension In Flight,"1997, [Online]. Available: www.fas.org/irp/program/collect/docs/ma_auvsi.html [Accessed: May 23, 2012]
- [9] S.P. Sane, "The aerodynamics of insect flight," *Journal of Experimental Biology*, Vol. 206, pp. 4191–4208, 2003.
- [10] T. Jardin, L. Chatellier, A. Farcy, and L. David, "Correlation between vortex structures and unsteady loads for flapping motion in hover," *Experiments in Fluids* Vol. 47, No.4–5, pp. 655–664, 2009.
- [11] M. Unal, J. Lin, and D. Rockwell, "Force prediction by PIV imaging: A momentum-based approach," *Journal of Fluids and Structures*, Vol. 11, No. 8, pp. 965–971, 1997.
- [12] F. Noca, D. Shiels, and D. Jeon, "A comparison of methods for evaluating time-dependent fluid dynamic forces on bodies, using only velocity fields and their derivatives," *Journal of Fluids and Structures*, Vol. 13, No.5, pp. 551–578, 1999.
- [13] S. Obi, and N. Tokai, "The pressure–velocity correlation in oscillatory turbulent flow between a pair of bluff bodies," *International Journal of Heat and Fluid Flow*, Vol. 27, No. 5, pp. 768–776, 2006.
- [14] A. Suryadi, and S. Obi, "The estimation of pressure on the surface of a flapping rigid plate by stereo PIV," *Experiments in Fluids*, Vol. 51, No. 5, pp. 1403–1416, 2011.
- [15] A. Suryadi, *The Phase-Averaged Velocity Field Measurement and the Estimation of Pressure Force on a Periodically Moving Body*. Thesis (PhD), Keio University, Japan, 2011.
- [16] A. Suryadi, T. Ishii, and S. Obi, "Stereo PIV measurement of a finite, flapping rigid plate in hovering condition," *Experiments in Fluids*, Vol. 49, No. 2, pp. 447–460, 2010.
- [17] S. Soloff, R. Adrian, and Z. Liu, "Distortion compensation for generalized stereoscopic particle image velocimetry," *Measurement Science and Technology*, Vol. 8, No. 12, pp. 1441–1454, 1997.
- [18] Kyowa Electronic Instruments Co., Ltd., Personal communication, 2008.
- [19] H. Coleman, and W. Steele, "Engineering application of experimental uncertainty analysis," *American Institute of Aeronautics and Astronautics Journal*, Vol. 33, No. 10, pp. 1888–1896, 1995.
- [20] C. Hunt, A. Wray, and P. Moin, "Eddies, streams and convergence zones in turbulent flows," In: *Studying Turbulence Using Numerical Simulation Databases, 2, Proceedings of the 1988 Summer Program (SEE N89-24538 18-34)*, pp. 193–208, 1988.